Materials Horizons

ROYAL SOCIETY OF CHEMISTRY

COMMUNICATION

View Article Online
View Journal

Check for updates

Cite this: DOI: 10.1039/d6mh00464d

Received 11th March 2026,
Accepted 6th May 2026

DOI: 10.1039/d6mh00464d

rsc.li/materials-horizons

Operando neutron radiography validates a parameter-free transport–kinetics model for thick solid-state battery cathodes†

Andre Adam, ‡[ab] Chanho Kim,‡[a] Yuanshun Li, [ac] Yuxuan Zhang,[d] Jean-Christophe Bilheux,[d] Xianglin Li, [be] Lei Cheng,[a] Hassina Bilheux [d] and Guang Yang *[af]

Tortuosity-weighted interfacial flux for lithium (TWIF-Li) predicts through-thickness Li gradients in thick composite all-solid-state cathodes without fitted parameters. Image-derived microstructures, GITT-derived concentration-dependent solid diffusion, and tortuosity-weighted interfacial kinetics reproduce *operando* neutron radiography across practical rates, delivering transferable design rules to suppress transport-limited reaction fronts.

All-solid-state batteries (ASSBs) are widely pursued as successor technologies to conventional Li-ion batteries, because replacing flammable liquid electrolytes with solid ion conductors can improve safety while enabling cell architectures with high energy density.[1,2] Realizing that promise at the cell level requires high-mass-loading, thick cathodes, since inactive components (electrolyte, current collectors, packaging) dilute material-level gains when electrodes remain thin.[3,4]

Recent experimental studies of practical-thickness solid-state cathodes show, however, that thicker composite cathodes often suffer pronounced losses in active-material utilization and exhibit strong spatial non-uniformity during cycling. Depth-profiling measurements on ~110 μm sulfide-composite cathodes, for example, report substantial lithiation gradients and link their evolution to high tortuosity—especially in the solid–electrolyte phase.[5] *Operando* neutron imaging further demonstrates that sluggish ion transport in composite cathodes can be rate limiting and can manifest as reaction-front-like behavior across the electrode thickness.[6] These observations underscore a central challenge for thick ASSB cathodes: performance is not governed by "average" transport properties alone, but by the coupled availability of ionic and electronic pathways and the localized kinetics at solid–solid contacts.

Modeling is essential for transforming these observations into actionable design rules. Classical porous-electrode theory, pioneered by Newman and collaborators, provides a powerful continuum framework for electrode-scale prediction and remains foundational in battery modeling. Yet the strength of this

New concepts

In this work, we introduce Tortuosity-weighted interfacial flux for lithium (TWIF-Li), a physically interpretable, parameter-free framework that predicts lithium transport and reaction heterogeneity in thick composite all-solid-state battery cathodes. The model integrates image-derived electrode microstructures, concentration-dependent solid-state diffusion extracted from GITT, and tortuosity-weighted interfacial kinetics. Importantly, the framework is directly validated by *operando* neutron radiography, demonstrating that it can reproduce through-thickness lithium gradients at practical current densities without fitting to cycling data. We believe this study offers a clear conceptual advance beyond incremental performance optimization. Rather than treating transport non-uniformity in thick solid-state cathodes as an empirical limitation, this work establishes a transferable physics-based framework that links microstructure, pathway tortuosity, interfacial kinetics, and spatial utilization in a predictive manner. The results also yield actionable design principles for suppressing transport-limited reaction fronts, including reducing mismatch between ionic and electronic pathway tortuosity and improving the uniformity of active interfaces. We expect these insights to be broadly relevant to researchers working on solid-state batteries, electrochemical materials, transport in heterogeneous solids, and *operando* characterization.

[a] *Chemical Sciences Division, Oak Ridge National Laboratory, Oak Ridge, USA. E-mail: yangg@ornl.gov*
[b] *Department of Mechanical Engineering, The University of Kansas, Lawrence, USA*
[c] *Department of Chemical and Biomolecular Engineering, University of Tennessee Knoxville, Knoxville, USA*
[d] *Neutron Scattering Division, Oak Ridge National Laboratory, Oak Ridge, USA*
[e] *McKelvey School of Engineering, Washington University in St. Louis, St. Louis, USA*
[f] *Bredesen Center for Interdisciplinary Research and Education, University of Tennessee Knoxville, Knoxville, USA*

‡ These authors contributed equally to this work.

framework—its ability to render complex microstructures tractable—comes from macrohomogeneous approximations that are not automatically valid for thick composite ASSB cathodes. Newman & Tobias' seminal analysis treats porous electrodes *via* a continuum macrohomogeneous approach that uses average quantities and effective transport properties, avoiding a detailed depiction of exact geometry and adopting homogeneous pore/interfacial-area concepts at the electrode scale.[7] Newman & Tiedemann similarly emphasize that practical porous-electrode models must capture the essential features of real electrodes without exact geometric detail, relying on parameters such as porosity, average surface area per unit volume, and volume-average resistivity.[8] In the Doyle–Fuller–Newman lineage of insertion-electrode modeling, insertion dynamics may be simplified using superposition, and parameterizations often assume large, constant electronic conductivity and constant solid diffusion coefficients together with a single characteristic particle size.[9] Modern assessments of DFN-style modeling reinforce this division of labor: homogenized DFN models can match averaged cell metrics efficiently, but microstructurally resolved models are needed to access localized dynamics and heterogeneities that drive degradation and non-uniform utilization.[10,11]

Thick ASSB cathodes stress these assumptions in multiple, coupled ways. First, unlike many liquid-electrolyte electrodes where electronic conductivity is engineered to be uniformly high, solid-state composite cathodes often operate as two interpenetrating and separately percolating networks: Li^+ transport through the solid electrolyte and electron transport through conductive additives and the active-material backbone. Spatial variability in solid–solid point contacts and ionic/electronic percolation pathways can therefore govern the reaction–transport coupling and the spatiotemporal evolution of electrochemical dynamics.[12] Second, solid-state composites can exhibit strong tortuosity and microstructure-dependent access to active interfaces, which makes local reaction localization sensitive to where ionic and electronic pathways are simultaneously favorable. Third, *operando* measurements of thick cathodes highlight that reaction non-uniformity is not merely an "edge effect": in high-mass-loading cathodes, *operando* neutron imaging directly visualizes non-uniform lithiation behavior and motivates architecture gradients because a uniform catholyte distribution can mismatch a non-uniform Li^+ flux field generated by faradaic reactions.[13] Together, these findings motivate a modeling closure that can connect microstructure-resolved pathway constraints to interfacial reaction rates under operating conditions.

Here, we introduce the Tortuosity-Weighted Interfacial Flux for Lithium (TWIF-Li), a parameter-free interfacial-kinetics relation that ties the local reaction rate at active-material–solid–electrolyte (AM–SE) contacts to the simulated ionic and electronic tortuosity[14] of the composite, providing a physically grounded boundary condition for lithium flux. This step is conceptually distinct from conventional porous-electrode closures, where tortuosity is typically treated as an input to effective transport coefficients or approximated through simple porosity-based correlations. The active-material diffusion coefficient is assigned as a function of local state of charge from Galvanostatic Intermitted Titration Technique (GITT)[15] measurements to capture an approximated concentration-dependent solid-state transport. The electrode architecture is taken directly from image-based reconstructions (FIB-SEM), so transport and reaction emerge from non-ideal geometry rather than idealized spherical-particle packings. Recently, we reported a Si|LPSCl|-$LiNbO_3$-coated NMC811 solid-state battery architecture optimized for maximizing energy density and cycling stability through hybrid processing and interfacial diagnostics.[16] The objective of the present study is different. Here, we do not seek to improve the performance record of that platform; rather, we use the same well-characterized chemistry as a model system to develop and validate a parameter-free transport-kinetics framework for thick composite cathodes. By combining image-derived microstructures, GITT-derived concentration-dependent diffusion, and *operando* neutron radiography, we directly test how lithium transport and interfacial reaction non-uniformity evolve through the cathode thickness. Holding the chemistry fixed enables the transport physics to be isolated and yields broadly relevant design rules for thick all-solid-state cathodes that were outside the scope of our earlier performance-focused study.

Critically, the framework is directly validated against *operando* neutron radiography measurements of lithium distribution across the cathode thickness under practical current densities.

By reproducing the observed evolution of through-thickness Li gradients across rate regimes without fitting to cycling data, TWIF-Li closes a key gap between macrohomogeneous porous-electrode modeling and *operando*-observed non-uniformity in thick solid-state cathodes. The result is a transferable set of design rules: suppress charge-induced gradients by reducing mismatch between ionic and electronic pathway tortuosity, and expand the synchronous-utilization window *via* architecture and interface engineering informed by *operando*-validated physics.

Experimental methods, image processing, GITT procedures, and simulation details are provided in the SI.

The *operando* neutron radiography cell is shown in (Fig. 1a). A normalized neutron transmission image of such a pristine cell is shown in (Fig. 1b). Stainless steel plungers and Polytetrafluoroethylene (PTFE) are relatively transparent to neutrons, so they are brighter compared to the electrodes and electrolyte at the center. (Fig. 1c) shows average neutron transmission at 100% state of charge (SOC), 50% state of discharge (SOD), and the fully discharged state as a function of distance from top to bottom as shown in (Fig. 1b). (Fig. 1d) shows the relative changes in neutron attenuation coefficient in each pixel. Details on how cylindrical geometric variations are normalized can be found in Supplemental Information. Experiments were conducted at C/10 and C/5, with a mass loading of 30 mg cm^{-2} $LiNbO_3$-coated NMC811 AM particles on LPSCl SE. (Fig. 1(e) and (f)) show the polarization curves for the cycles where the data was collected.

The main objective of this study is to model the transport of Li^+ during a charge–discharge cycle and compare it with the neutron imaging data. Fig. 2 shows the three-phase representative volume element (RVE) for simulation, derived from

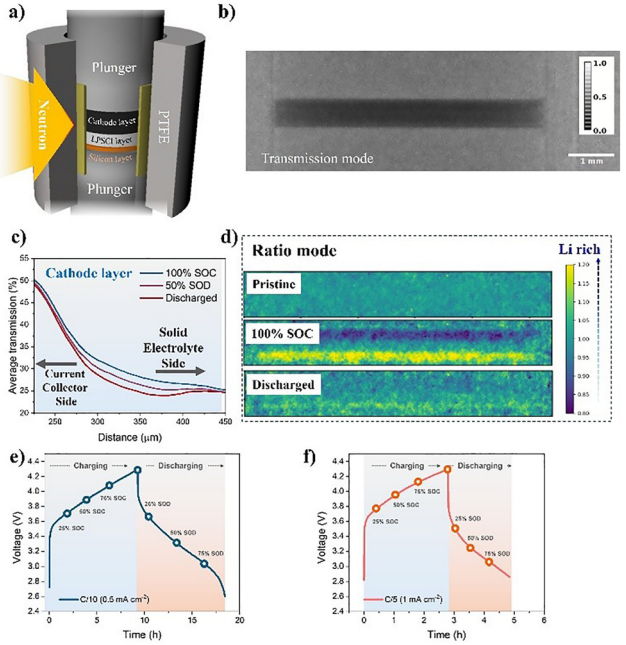

Fig. 1 (a) Drawing showing the cell configuration for *operando* neutron radiography. (b) Example of measured grayscale neutron transmission. (c) The transmission values are averaged for each row of pixels along the diameter of the cathode and can be plotted along the axis perpendicular to the battery to compare across SOCs. (d) Three images in ratio mode showing the ratio of attenuation coefficients (compared to a pristine state). Dark colors indicate lower presence of lithium, whose movement can be tracked during cycling. (e) and (f) include the polarization curves for the cycles at C/10 and C/5 respectively, for which the neutron radiographs were taken.

FIB-SEM images with a pixel resolution of 270 nm. The Li^+ concentration is assumed to be constant in the SE, since the transport in the SE phase is at least three orders of magnitude faster[17,18] than that in the AM.

The mass flux boundary condition is then applied at each AM-SE interface, which are referred to as active interfaces. For the inactive interfaces, the mass flux is always zero. In a system, Ω, with $n \times m = N$ control volumes $\Omega_{i,j}$, the total flux is given by J^*:

$$J^* = \frac{I_0}{zF\sum_{i,j}^{N} s_{i,j}} \quad (1)$$

here I_0 is the applied current density, $s_{i,j}$ is the active surface area of control volume (i,j), z is the charge number, and F is the Faraday constant. Fig. 2 displays the boundary conditions applied to the RVE.

The average in-plane lithium concentration is obtained from neutron imaging for a full cycle at 0.5 mA cm^{-2} and is shown in Fig. 3a). The lithium depletion profile is asynchronous in charging, with most of the depletion taking place at the center of the cathode, while the current collector side and the SE side see significantly less depletion.

In discharge, the profile is initially asynchronous, as most of the lithium replenishment occurred near the cathode center.

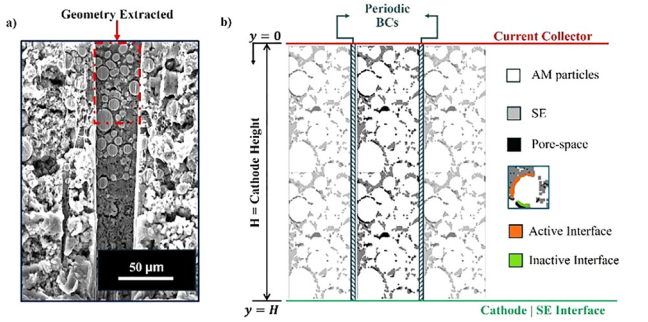

Fig. 2 (a) FIB-SEM of composite cathode cross-section. (b) The periodic boundary conditions for the three-phase system are shown, along with the boundary treatment for active *versus* inactive interfaces.

Then, as the lithium saturation becomes more even across the domain, the lithium-concentration profile transitions to a synchronous state, where the entire cathode seems to be at a similar SOD.

In order to model this asynchronous behavior, eqn (1) must be modified. We theorize that the depletion profile is a competition between transport pathways: the Li^+ ions must travel towards the anode, and e^- must travel to the current collector. Therefore, while a reaction near the current collector might be favorable to the electron transport, the Li^+ ion must cross the entire length of the cathode. The opposite is also true for a reaction happening closer to the anode. Therefore, the rate at which a reaction occurs can be thought of as a balance between the potential for ion and electron transfer, with the minima occurring at the current collector and the solid–electrolyte interface, respectively.

The availability of lithium in the active interface plays an important role in the overall reaction,[19] and therefore the mass flux at the interface. This term is especially important if the depletion is asynchronous, as the availability of Lithium changes drastically with position on the cathode, particle size, and diffusion coefficient. A weighting factor is added to eqn (1) to address the asynchronous accounting of lithium concentrations in the composite cathode during cycling:

$$J^*(t) = \sum_{i,j}^{N} W_{i,j} \frac{I_0}{zF\sum_{i,j}^{N} s_{i,j}} \quad (2)$$

where $W_{i,j}$ is the dimensionless weighing factor. At each control volume, $W_{i,j}$ from eqn (2) is expressed as the product of two factors, w_1 and w_2, given as follows:

$$w_1(y) = 2\left[1 - \frac{\left(\tau_{e^-|AM} \cdot d_{cc} - \tau_{Li^+|SE} \cdot d_{SE}\right)^2}{\left(\tau_{max} \cdot H\right)^2}\right] \quad (3)$$

$$w_2(x,y,t) = \sqrt{\frac{c_{i,j}(t)}{c_{sat}}} \quad (4)$$

where $\tau_{e^-|AM} \cdot d_{cc}$ is an estimate of the diffusion pathway for the electron towards the current collector, $\tau_{Li^+|SE} \cdot d_{SE}$ is an estimate of the lithium diffusion pathway towards the separator, $\tau_{max} \cdot H$

is the longest possible diffusion pathway in the domain, for a cathode with height H. The tortuosity calculation is shown in section 4.4 of the SI. The term w_1 is a function of the distance from the current collector d_{cc} and $d_{cc} = H - d_{SE}$.

In w_2, c_{sat} is the concentration of lithium in the AM at a pristine state, and $c_{i,j}(t)$ is the concentration of lithium in control volume $\Omega_{i,j}$, at time t. The rationale for this simulation setup can be found in the SI (Section S4 and S5).

In eqn (3), all terms refer to the geometry of the composite cathode and are time invariant. Conversely, $c_{i,j}$ in eqn (4) is time-dependent, therefore representing a dynamic component of the reaction rate response to the available lithium in the AM. Thus, both w_1 and w_2 are dependent on location, (i,j), but only w_2 needs to be re-evaluated at each time-step.

Based on eqn (4), the lithium concentration at the active interfaces has a significant effect on the flux at that interface. In order to correctly simulate this phenomenon, it is paramount to use the correct diffusion coefficient for lithium in the cathode AM. From GITT, we know that the $D_{Li|AM}$ can vary by several orders of magnitude based on SOC. On the other hand, it is clear from (Fig. 3d) that the cathode has significant concentration gradients, and therefore ascribing the same "SOC" to the AM particles on a microstructural level has no physical meaning.

A new interpretation of GITT is proposed: the data, allied to the neutron imaging experiment, is interpreted as a function of the average concentration. This interpretation is then used to fit the theory of anomalous diffusion,[20] which is stated in eqn (5):

$$D' = D_{trace}\frac{c_{Li,max} + c_{Li}}{c_{Li,max} - c_{Li}} \quad (5)$$

where D_{trace} is the diffusion coefficient in the AM when present at low concentrations (trace amounts), and $c_{Li,max}$ is the saturation lithium concentration in the cathode. Both parameters are derived based on the GITT data shown in Section S3 of the SI. Note that each control volume at each time step will have a different diffusion coefficient assigned, as $D'_{i,j}$ is a function of the local concentration, $c_{i,j}$.

(Fig. 3b) shows a simulation of the model proposed in eqn (2), and can be directly compared to the neutron imaging data in (Fig. 3a). Both are constructed using the average lithium concentration across the thickness of the cathode, with a frame taken every 5 minutes, a limitation imposed by the neutron imaging experiment. For the charge cycle, $W_{i,j}$ is used for the reaction rate, while in the discharge cycle the deposition is best described by the complement w_2 alone, since the tortuosity dependence does not appear to play a significant role in discharge.

Overall, the model for depletion proposed in eqn (2) shows good qualitative agreement with the delithiation profile derived experimentally. At 100% SOC, the model predicts an average depletion of 51.2%, while the data show an average of 53.2% depletion across the cathode. The model also captures the highly inhomogeneous and asynchronous nature of this depletion revealed by the experiment. A detailed quantitative analysis of the error between simulation and experiment is provided in the SI.

During discharge, the model based on eqn (4) shows similar dynamic behavior to the data. Initially, lithium preferentially replenishes areas with lower concentrations. However, when the concentration profile is approximately even, the cathode seems to be replenished with lithium in a more even fashion. The model correctly captures the evolution from asynchronous-to-synchronous discharge, although lithium loss, which is attributed to the plating in the anode, is not modeled, hence the discrepancy.

Fig. 4(a) shows the neutron imaging data during a charge–discharge cycle with higher current density. During charge, the cathode exhibits a asynchronous behavior similar to that shown in Fig. 3. However, during discharge at high C-rate, the behavior is always roughly asynchronous and does not transition to a synchronous state of lithium concentration in the cathode.

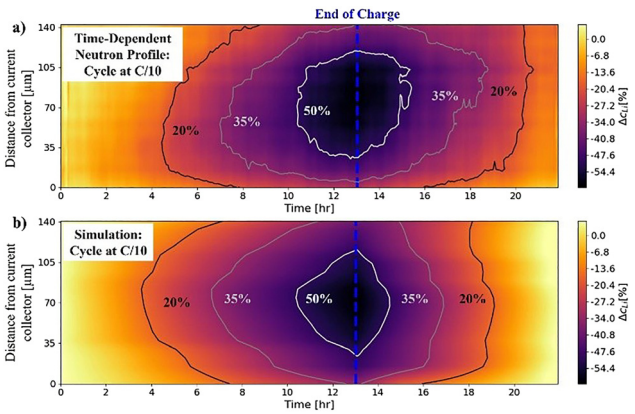

Fig. 3 (a) Time-dependent lithium concentration profile as a function of the cathode height estimated from the neutron transmission profiles for a charge–discharge cycle at C/10. (b) Simulation of cathode charge and discharge with the same applied current and temporal resolution as the experiment.

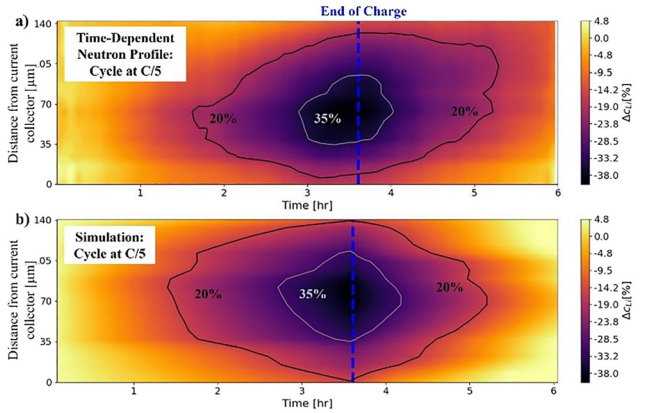

Fig. 4 (a) Time-dependent lithium concentration profile as a function of the cathode height estimated from the neutron transmission profiles for a charge–discharge cycle at C/5. (b) Simulation of cathode charge and discharge with the same applied current and temporal resolution as the experiment.

The simulation in (Fig. 4b) shows a very similar behavior to the data in (Fig. 4a), with asynchronous charge and discharge mechanisms. Critically, the simulation does not have any parameters that are fitted to a specific cathode chemistry, and the only difference between the simulations in (Fig. 3b) and (Fig. 4b) is the applied current, I_0, in eqn (2).

Further simulations are shown for practical C-rates of C/25 and C/8.3 in Fig. 5(a) and (b), respectively.

Although these simulations are not directly validated by neutron radiography, using the same TWIF-Li model supports the hypothesis that the transition from synchronous to asynchronous occurs naturally, due to an intrinsic kinetic limitation at higher current densities. In Fig. 5(a), the lithiation gradients during charge are the most synchronous out of all the simulations, suggesting the asynchronous behavior emerges from a progressive kinetic limitation. Fig. 5(b) shows a simulation with C/8.3, an intermediate value between Fig. 3(b) and Fig. 4(b). In this case, the asynchronous behavior during discharge is already observed, albeit less prominent than in Fig. 4(b).

The results presented herein, allied with the observation of the transition from asynchronous to synchronous behavior in Sharma, Vasconcelos, and Zhao[21] at low C-rates, suggests that the inhomogeneities are due to limitations in reaction kinetics. The inhomogeneities are more pronounced at higher C-rates, where the kinetics are a major performance bottleneck.

TWIF-Li also aligns well with data from other publications,[5,6,13] suggesting that the tortuosity dependence of the asynchronous concentration distributions in thick cathodes are a more general feature, rather than a specific observation from our study. As more data become available for different systems and chemistries of ASSBs, the bounds of validity for TWIF-Li will become more apparent.

To summarize, we introduced TWIF-Li, a parameter-free, physically interpretable framework for lithium transport in composite ASSB cathodes that (i) casts GITT data into an anomalous diffusion form to obtain concentration dependent solid-state diffusion, and (ii) defines a tortuosity-weighted interfacial flux relation that links local reaction rates at active-material/solid–electrolyte (AM–SE) contacts to the measured ionic and electronic pathway tortuosity. Using image-informed, non-ideal microstructures and no fitting to cycling data, TWIF-Li quantitatively reproduces *operando* neutron radiography measurements of through-thickness lithium distributions across practical rate regimes.

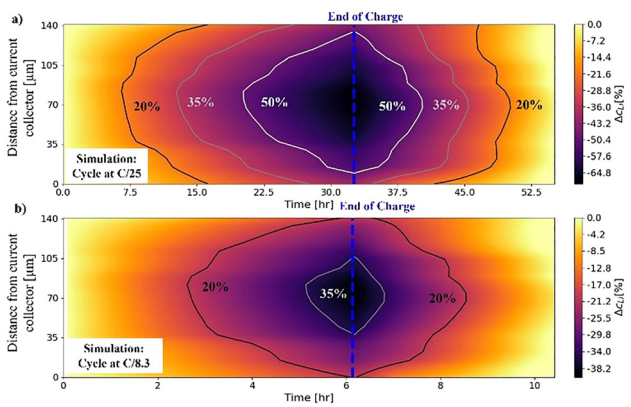

Fig. 5 Simulation of lithium distribution on the cathode during charge and discharge for practical current densities of (a) C/25 and (b) C/8.3.

Mechanistic insights

• Asynchronous charge emerges from tortuosity imbalance. Reaction hot spots form where ionic and electronic percolation are both favorable, leading to lithium depletion gradients during charge.

• Low-rate discharge tends toward synchronicity. As the positive electrode approaches higher saturation, discharge rates stabilize, indicating the state of saturation, rather than the spatial position, governs the kinetics at sufficiently low current density.

• Higher charge and discharge rates lead to widespread concentration heterogeneity. Persistent post-charge/discharge concentration inhomogeneities at higher current densities reflect locally slow interfacial kinetics and imbalanced percolation, explaining efficiency losses and incomplete utilization.

Design implications

• Balance the networks. Co-optimize ionic and electronic tortuosity (reduce their mismatch) to suppress charge-induced gradients and expand the synchronous-operation window.

• Engineer interfaces, not just thickness. Increase uniform, effective AM–SE contact (*via* binder/SE distribution, coatings, or processing) to raise local interfacial rates where pathways are limiting.

• Tune particle and architecture scales. Adjust active-particle size distributions, phase fractions, and connectivity to keep the electrode within the synchronous regime boundary identified by TWIF-Li at target areal loadings and currents.

• Use physics-only predictions to scale. Because TWIF-Li is parameter-free and *operando*-validated, it provides transferable design rules for diverse chemistries and architectures, enabling rational scaling to higher-energy cathodes without trial-and-error fitting.

• TWIF-Li closes a key gap by unifying spatial distribution, dynamics, and interfacial reaction kinetics in a single, predictive framework that is backed by *operando* neutron radiography—delivering practical guidance for building higher-loading, higher-efficiency ASSB cathodes.

Author contributions

A. A., C. K. Conceptualization, data curation, formal analysis, validation, investigation, methodology, writing: original draft, writing: review & editing. A. A. Software, visualization. Y. L. Formal analysis, validation, writing – review & editing. Y. Z., H. B., and J. C. B. Resources, methodology, data curation, validation, writing – review & editing. X. L., and L. C. Data curation, formal analysis, writing: review & editing. G. Y. Conceptualization, data curation, validation, investigation, formal analysis,

funding acquisition, project administration, supervision, resources, writing: review & editing.

Conflicts of interest

There are no conflicts to report.

Data availability

Additional details regarding experimental procedures, processing of the neutron data, and simulation parameters are included in the supplementary information (SI). The code used for this project is publicly available at https://github.com/adama-wzr/EffectiveDiffusivityFVM. See DOI: https://doi.org/10.1039/d6mh00464d.

Acknowledgements

This research was conducted at the Oak Ridge National Laboratory, managed by UT Battelle, LLC for the U.S. Department of Energy (DOE) and is sponsored by the Office of Critical Minerals and Energy Innovation (CMEI) in the Transportation Technologies Office (TTO) through the Advanced Battery Materials Research (BMR) Program, managed by Dr Simon Thompson and Mr Tien Duong. This manuscript has been authored by UT Battelle, LLC under Contract No. DE-AC05-00OR22725 with the U.S. Department of Energy. We acknowledge that this research was supported in part by an appointment to the Oak Ridge National Laboratory GRO Program, sponsored by the U.S. Department of Energy and administered by the Oak Ridge Institute for Science and Education. The diffusion model was in part developed on the Expanse (GPU) at San Diego Supercomputer Center through allocations MAT210014 and MAT230071 from the Advanced Cyberinfrastructure Coordination Ecosystem: Services & Support (ACCESS) program, which is supported by National Science Foundation grants 2138259, 2138286, 2138307, 2137603, and 2138296. Part of this research used resources at the High Flux Isotope Reactor and the Spallation Neutron Source, a DOE Office of Science User Facility operated by the Oak Ridge National Laboratory. The beam time was allocated to MARS on proposal number IPTS-34509.1 and to VENUS on IPTS-35566.SEM research was conducted as part of a user project at the Center for Nanophase Materials Sciences (CNMS) (Proposal number: CNMS2025-A-02967), which is a US Department of Energy, Office of Science User Facility at Oak Ridge National Laboratory. We thank Dr Jagjit Nanda from SLAC National Accelerator Laboratory and Dr James R Torres from High Flux Isotope Reactor, Neutron Science at ORNL for the fruitful discussions.

References

1 G. Whang and W. G. Zeier, *ACS Energy Lett.*, 2023, **8**, 5264–5274.
2 J. Janek and W. G. Zeier, *Nat. Energy*, 2023, **8**, 230–240.
3 G. Yang, *Mater. Horiz.*, 2025, **12**, 315–316.
4 Y. Li, Y. Cho, J. Cai, C. Kim, X. Zheng, W. Wu, A. L. Musgrove, Y. Su, R. L. Sacci, Z. Chen, J. Nanda and G. Yang, *Mater. Horiz.*, 2025, **12**, 119–130.
5 A. M. Stavola, X. Sun, D. P. Guida, A. M. Bruck, D. Cao, J. S. Okasinski, A. C. Chuang, H. Zhu and J. W. Gallaway, *ACS Energy Lett.*, 2023, **8**, 1273–1280.
6 R. Bradbury, G. F. Dewald, M. A. Kraft, T. Arlt, N. Kardjilov, J. Janek, I. Manke, W. G. Zeier and S. Ohno, *Adv. Energy Mater.*, 2023, **13**(17), 2203426.
7 E. J. Podlaha, H. Deligianni and G. Stafford, *Electrochem. Soc. Interface*, 2010, **19**, 39–42.
8 J. Newman and W. Tiedemann, *AIChE J.*, 1975, **21**, 25–41.
9 T. F. Fuller, M. Doyle and J. Newman, *J. Electrochem. Soc.*, 1994, **141**, 1–10.
10 E. C. Tredenick, A. M. Boyce, S. Wheeler, J. Li, Y. Sun, R. Drummond, S. R. Duncan, P. S. Grant and P. R. Shearing, *J. Electrochem. Soc.*, 2025, **172**, 030503.
11 C. D. Parke, L. Teo, D. T. Schwartz and V. R. Subramanian, *Sustainable Energy Fuels*, 2021, **5**, 5946–5966.
12 K. G. Naik, B. S. Vishnugopi and P. P. Mukherjee, *ACS Appl. Mater. Interfaces*, 2022, **14**, 29754–29765.
13 T. Ji, Y. Zhang, J. Torres, A. S. Mijailovic, Y. Tang, X. Zhao, J.-C. Bilheux, J. Wang, B. W. Sheldon, O. Oyedeji and H. Zhu, *Nat. Commun.*, 2025, **16**, 7667.
14 S. J. Cooper, A. Bertei, P. R. Shearing, J. A. Kilner and N. P. Brandon, *SoftwareX*, 2016, **5**, 203–210.
15 M. Jia, W. Zhang, X. Cai, X. Zhan, L. Hou, C. Yuan and Z. Guo, *J. Power Sources*, 2022, **543**, 231843.
16 C. Kim, Y. Li, I. Jang, W. Wu, Y. Su, H. M. Meyer, J. Keum, J. Nanda and G. Yang, *Adv. Mater.*, 2025, **37**(27), 2502300.
17 R. Schlenker, A.-L. Hansen, A. Senyshyn, T. Zinkevich, M. Knapp, T. Hupfer, H. Ehrenberg and S. Indris, *Chem. Mater.*, 2020, **32**, 8420–8430.
18 C. Kim, Y. Li, A. Adam, W. Wu, G. Parker, I. Jang, Y. Ahn, Y. F. Su, H. M. Meyer, X. Y. Yu, J. Nanda and G. Yang, *Energy Storage Mater.*, 2026, **86**, 105009.
19 A. J. Bard and L. R. Faulkner, *Electrochemical methods: fundamentals and applications*, John Wiley & Sons, Inc., 2001.
20 P. E. Bakeman and J. M. Borrego, *J. Electrochem. Soc.*, 1970, **117**, 688.
21 N. Sharma, L. S. De Vasconcelos, S. Hassan and K. Zhao, *Nano Lett.*, 2022, **22**, 5883–5890.

